Available online at www.sciencedirect.com
SCIENCE DIRECT®
Ocean Modelling 11 (2006) 347–375
Ocean Modelling
www.elsevier.com/locate/ocemod

Formulation, implementation and examination of vertical coordinate choices in the Global Navy Coastal Ocean Model (NCOM)

Charlie N. Barron *, A. Birol Kara, Paul J. Martin, Robert C. Rhodes, Lucy F. Smedstad

Oceanography Division, Naval Research Laboratory, Code 7322, Bldg. 1009, Stennis Space Center, MS, USA

Received 19 April 2004; received in revised form 14 January 2005; accepted 14 January 2005
Available online 16 February 2005

Abstract

A 1/8° global version of the Navy Coastal Ocean Model (NCOM) is described with details of its formulation, implementation, and configuration of the vertical coordinate. NCOM is a baroclinic, hydrostatic, Boussinesq, free-surface ocean model that allows its vertical coordinate to consist of σ coordinates for the upper layers and z-levels below a user-specified depth. This flexibility allows implementation of a hybrid σ–z coordinate system that is expected to mitigate some of the weaknesses that can be associated with either pure coordinate option. For the global NCOM application, the σ–z coordinate is used to allow terrain-following σ coordinates in the upper ocean, providing better resolution and topographic fidelity in shelf regions where flow is most sensitive to its representation. Including z coordinates for deeper regions efficiently maintains high near-surface vertical resolution in the open ocean. Investigation into the impact of the selected coordinate system focuses on differences between atmospherically-forced free-running (no assimilation) global solutions using σ–z and pure z coordinates. Comparisons with independent temperature observations indicate that global NCOM using the σ–z coordinate has improved skill relative to its z coordinate implementation. Among other metrics, we show that in comparison with time series of surface temperature from National Oceanic Data Center (NODC) buoys, mostly located in coastal regions, root mean squared differences (RMSD) improved for 63% and correlation improved for 71% of the stations

* Corresponding author. Tel.: +1 228 688 5437.
E-mail addresses: barron@nrlssc.navy.mil (C.N. Barron), kara@nrlssc.navy.mil (A.B. Kara), martin@nrlssc.navy.mil (P.J. Martin), rhodes@nrlssc.navy.mil (R.C. Rhodes), lsmedstad@nrlssc.navy.mil (L.F. Smedstad).

1463-5003/$ - see front matter Published by Elsevier Ltd.
doi:10.1016/j.ocemod.2005.01.004

when σ–z coordinates were used instead of pure z. For the exclusively open-ocean Tropical Atmosphere-Ocean (TAO) buoys, differences between the simulations were small, with the σ–z showing smaller RMSD for 45% of the stations and higher correlation for 65% of the stations. Additional comparisons using temperature profile observations further confirm a tendency for improved performance using the hybrid σ–z coordinates.
Published by Elsevier Ltd.

Keywords: Coastal ocean model; NCOM; Vertical Grid; z-level; σ Coordinate; Optimal coordinate

1. Introduction

A 1/8° global version of the Navy Coastal Ocean Model (NCOM) has been developed by the Naval Research Laboratory (NRL) and transitioned to begin operations at the Naval Oceanographic Office (NAVOCEANO). NCOM is a result of efforts to standardize model development at NRL, leading to more efficient configuration management and reduced duplication of effort for transition and support of models implemented for Naval operations. This paper covers the formulation of NCOM, its global implementation, and a comparison of results arising from different choices of the vertical coordinate system. Additional information on global NCOM is provided by Rhodes et al. (2002), Barron et al. (2004), and Kara et al. (this issue).

Entities that are engaged in global maritime operations have an interest in real-time mesoscale analyses and forecasts over the global ocean. Properties of interest include sea level, temperature, salinity, and currents. From these, additional properties such as transport, density and sound speed may be derived. For operational applicability, this information must be available at short notice anywhere on the globe. Ideally, the data would be provided with reasonable accuracy and meaningful uncertainty estimates. If higher resolution information is needed, the global data should support nesting of relocatable models.

A variety of resources are utilized to operationally provide global ocean information. Satellite observations are invaluable for analyses of the ocean surface. However, the relatively fine spatial and temporal resolution of satellite surface observations is not generally available for the interior of the ocean. Direct subsurface measurements tend to be too sparse and widely scattered to resolve ocean features over most of the ocean. Ocean General Circulation Models (OGCMs) help compensate for the sparseness of oceanic observations by providing dynamic interpolation of the available data. Thus, they play an important role in representing the ocean component of the climate system on a wide variety of temporal and spatial scales.

There are a variety of OGCMs in general use. One of the most definitive ways to distinguish OGCMs that use finite differences in the horizontal is by their choice of vertical discretization. Lagrangian and isopycnal layer models have primarily been used in deep-water modeling (Hurlburt and Thompson, 1980; Bleck et al., 1992), and in predicting climatological and interannual sea surface temperature with relatively low vertical resolution as well (Kara et al., 2004, 2003). Recent developments have shown broader application and highlighted the benefits of isopycnal layers within hybrid coordinates (Bleck, 2002; Chassignet et al., 2003; Halliwell, 2004). These models are efficient in describing mesoscale ocean circulation in which the mesoscale dynamics are dependent mainly upon a few vertical modes. The layer formulation of these models helps reduce

spurious numerical diffusion in the vertical, and isopycnal models minimize spurious cross-isopycnal mixing caused by horizontal diffusion when the isopycnal surfaces are not aligned with the surfaces defined by the vertical coordinate. Layer models have difficulty handling overturning circulations, and the intersection of the layers with the ocean bottom or the ocean surface causes complications. Isopycnal models can encounter difficulty in situations where different water masses mix and become ill-defined, e.g., during deep-water convection or vertical mixing in shallow water.

While a layer model pursues discretization according to the properties and time-varying thickness of each layer, level models typically mark the water at depths that are fixed relative to the bottom, the z-level approach, or that are a fixed fraction of the total water depth, the σ coordinate approach. Isopycnic models are discrete in density, while non-adaptive (z, σ) coordinate models are continuous in density. In general, σ coordinates have been popular in shallow-water and coastal modeling because of their ability to follow the bathymetry and thereby provide more consistent vertical resolution within the bottom boundary layer. They also naturally provide increased vertical resolution in shallow water. However, ocean models with σ coordinates can suffer significant errors in their horizontal pressure gradient, advection, and diffusion terms in regions of abrupt changes in depth (e.g., Martin, 1985; Deleersnijder and Beckers, 1992; Paul, 1994; Ezer et al., 2002).

Alternatively, z-level coordinates may be favored for allowing simple calculation of the horizontal pressure gradient and avoiding truncation errors that can be encountered in calculating this term along steeply sloping coordinate surfaces. Vertical resolution at a particular depth is constant, which provides control of minimum vertical resolution in deep-water regions. But z-level coordinates can suffer from inaccuracy in representing the bottom depth if the bottom depth is rounded to the nearest z-level, and they cannot provide locally increased resolution in the bottom boundary layer or in shallow water without the expense of increased resolution over the entire domain. Memory may also be wasted accounting for inactive points below the ocean floor.

Additional refinements to the model formulation with either σ or z coordinates can mitigate their deficiencies at various levels of increased computational cost. A detailed examination of a broad variety of methodologies which may be employed is beyond the scope of this paper. We present results using the hybrid σ–z coordinate, an approach accommodated by NCOM that is designed to capitalize on some of the advantages and avoid some of the difficulties posed by the traditional coordinates. These results are compared with NCOM run using z coordinates with a free surface to illustrate some effects of coordinate system choices.

The purposes of NCOM in general and global NCOM in particular include support of multiple ocean nests and coupling with atmospheric models to better represent air–sea interactions, in addition to providing stand-alone ocean nowcasts and forecasts. In its global configuration, which is undergoing operational testing at NAVOCEANO, NCOM will provide three- to five-day forecasts and host an embedded Arctic ice model in addition to supporting various higher-resolution nested ocean models.

This paper is organized as follows: Section 2 describes the basic physics, numerics, and computational procedures used in NCOM. Section 3 describes the model setup for global simulations. Section 4 provides some comparisons of the use of pure z-level, and σ–z (hybrid) coordinates in NCOM. Section 5 discusses the impact of coordinate system choice on subsurface temperatures, and Section 6 offers some conclusions and directions for further research.

2. NCOM description

The physics and numerics of NCOM are based largely on the Princeton Ocean Model (POM) as described in Blumberg and Mellor (1987), with some aspects from the Sigma/Z-level Model (SZM) (Martin, 2000), and with some additional features. POM is a three-dimensional, primitive equation, baroclinic, hydrostatic and free surface model. It uses an orthogonal-curvilinear horizontal grid, a σ (i.e., bottom-following) vertical grid, a split–explicit treatment of the free surface, Smagorinsky horizontal mixing, and the Mellor-Yamada Level 2.5 turbulence model for vertical mixing. SZM is similar in many ways to POM, but differs from POM in that it uses a Cartesian horizontal grid (the grid spacing in the horizontal is constant), a combined σ/z-level vertical grid, an implicit treatment of the free surface, horizontal eddy coefficients calculated based on a maximum grid-cell Reynolds number criteria, and vertical eddy coefficients calculated using the Mellor-Yamada Level 2 turbulence closure scheme. Primitive equations and the finite differencing and computational procedures used in NCOM are provided here, in detail.

2.1. NCOM physics

NCOM has a free surface and is based on the primitive equations and the hydrostatic, Boussinesq, and incompressible approximations. The basic equations are given in the Cartesian coordinate system as follows:

Continuity:

$$\frac{\partial u}{\partial x}+\frac{\partial v}{\partial y}+\frac{\partial w}{\partial z}=Q, \tag{1}$$

Momentum:

$$\frac{\partial u}{\partial t}+\nabla\cdot(\mathbf{v}u)=-\frac{1}{\rho_0}\frac{\partial p}{\partial x}+fv+Qu+\nabla_{\mathrm{H}}(A_{\mathrm{M}}\nabla_{\mathrm{H}}u)+\frac{\partial}{\partial z}\left(K_{\mathrm{M}}\frac{\partial u}{\partial z}\right), \tag{2}$$

$$\frac{\partial v}{\partial t}+\nabla\cdot(\mathbf{v}v)=-\frac{1}{\rho_0}\frac{\partial p}{\partial y}-fu+Qv+\nabla_{\mathrm{H}}(A_{\mathrm{M}}\nabla_{\mathrm{H}}v)+\frac{\partial}{\partial z}\left(K_{\mathrm{M}}\frac{\partial v}{\partial z}\right), \tag{3}$$

Temperature:

$$\frac{\partial T}{\partial t}+\nabla\cdot(\mathbf{v}T)=QT+\nabla_{\mathrm{H}}(A_{\mathrm{H}}\nabla_{\mathrm{H}}T)+Q_{\mathrm{r}}\frac{\partial\gamma}{\partial z}+\frac{\partial}{\partial z}\left(K_{\mathrm{H}}\frac{\partial T}{\partial z}\right), \tag{4}$$

Salinity:

$$\frac{\partial S}{\partial t}+\nabla\cdot(\mathbf{v}S)=QS+\nabla_{\mathrm{H}}(A_{\mathrm{H}}\nabla_{\mathrm{H}}S)+\frac{\partial}{\partial z}\left(K_{\mathrm{H}}\frac{\partial S}{\partial z}\right), \tag{5}$$

Elevation:

$$\frac{\partial\zeta}{\partial t}=\frac{\partial[(\zeta+H)\bar{u}]}{\partial x}-\frac{\partial[(\zeta+H)\bar{v}]}{\partial y}, \tag{6}$$

Hydrostatic:

$$\partial p/\partial z = -\rho g, \tag{7}$$

where

$$\rho = \rho(T, S, z),$$
$$f = 2\Omega \sin(\theta),$$
$$\nabla = \hat{\mathbf{i}}\frac{\partial}{\partial x} + \hat{\mathbf{j}}\frac{\partial}{\partial y} + \hat{\mathbf{k}}\frac{\partial}{\partial z},$$
$$\nabla_{\mathrm{H}} = \hat{\mathbf{i}}\frac{\partial}{\partial x} + \hat{\mathbf{j}}\frac{\partial}{\partial y}.$$

In the equations above, Q is a volume source/sink term that can be used to specify source and sink flows such as river and runoff inflows, f is the Coriolis parameter, Q_{r} is the solar radiation penetrating the surface, and γ is the solar extinction profile (Martin and Allard, 1993). Parameters appearing in these equations and symbols throughout the text are briefly described in Appendix A. The form of these equations in σ coordinates is given in Blumberg and Mellor (1987, 1983). The form of the σ coordinate equations used in NCOM is similar to that presented by Blumberg and Mellor (1987) except that the depth in the equations is replaced by $\min(H, z_s)$, where z_{s} is the depth at which the grid changes from σ- to z-level coordinates.

The surface boundary conditions for the above equations are the surface stress for the momentum equations, the surface heat flux for the temperature equation, and the effective surface salt flux for the salinity equation. The bottom boundary conditions are the bottom drag for the momentum equations, which is parameterized by a quadratic drag law, and zero flux for the temperature and salinity equations.

The horizontal mixing coefficients (A_{M} and A_{H}) as parameterized in Section 2.3 can be calculated with the Smagorinsky (1963) scheme or a grid-cell Reynolds number scheme where the mixing coefficients are determined from a specified grid-cell Reynolds number. Minimum values for the coefficients can be specified for both schemes.

The vertical mixing coefficients K_{M} and K_{H} are calculated using the Mellor-Yamada Level 2 (Mellor and Yamada, 1974) or Level 2.5 (Mellor and Yamada, 1982) turbulence models. For the Level 2 model, the turbulent length scale is set to zero outside of turbulent layers, and within turbulent layers is computed as $((kz_{\mathrm{t}})^{-1} + (kz_{\mathrm{b}})^{-1})^{-1}$, where z_{t} and z_{b} are the distances to the upper and lower boundaries of the turbulent layer, respectively, and k is von Kármán's constant. However, at the surface and bottom the turbulent length scales for both models asymptote to k times the roughness scale at the boundary. The Level 2 model can optionally include the Richardson-number based mixing enhancement scheme of Large et al. (1994), which provides for weak mixing at the edge of a turbulent boundary layer for Richardson numbers above the normal critical value of about 0.25 up to a value of 0.7. For the Level 2.5 scheme, the surface flux of turbulent kinetic energy can be specified as in Craig and Banner (1994).

Density is computed using the Friedrich and Levitus (1972) polynomial approximation of the equation of state or the adaptation by Mellor (1991) of the United Nations Educational Scientific and Cultural Organization (UNESCO) equation of state (Millero et al., 1980; Millero and Poisson, 1981).

2.2. NCOM numerics

The model equations are solved on an Arakawa C grid, and the horizontal grid is orthogonal curvilinear as in POM (Blumberg and Herring, 1987). A distinguishing feature of NCOM is its vertical grid, which uses σ coordinates from the surface down to a user-specified depth (z_s) and z-levels below. The σ grid is divided into layers as in POM, with each σ-layer being a fixed fraction of the total depth occupied by the σ-layers. On the z-level grid, the bottom depth is rounded to the nearest z-level.

Fig. 1 illustrates the different ways the grid can be configured. One extreme is a vertical grid with a single σ-layer at the surface and z-levels below (Fig. 1a). Since the model has a free surface, at least one σ-layer is needed to allow for changes in the surface elevation. If the changes in the surface elevation are large relative to the grid resolution desired near the surface, a single σ-layer may not be sufficient to resolve the perturbations in the surface elevation. To address this contingency, several σ-layers may be used in the upper portion of the water column, allowing fractional distribution of variations in surface elevation among each. (Fig. 1b).

For water depths shallower than the z_s transition depth from σ-layers to z-levels, the σ-layers extend to the bottom and become more concentrated as depth decreases, maintaining spacing that is a constant fraction of the water column. Fig. 1c shows a grid in which σ-layers extend to the bottom over the shelf, and z-levels represent the deeper water off the shelf. A grid in which σ-layers are used all the way to the bottom everywhere is also possible (Fig. 1d). Over deep water, restricting σ-layers to the upper portion provides better control on the uniformity of near-surface resolution.

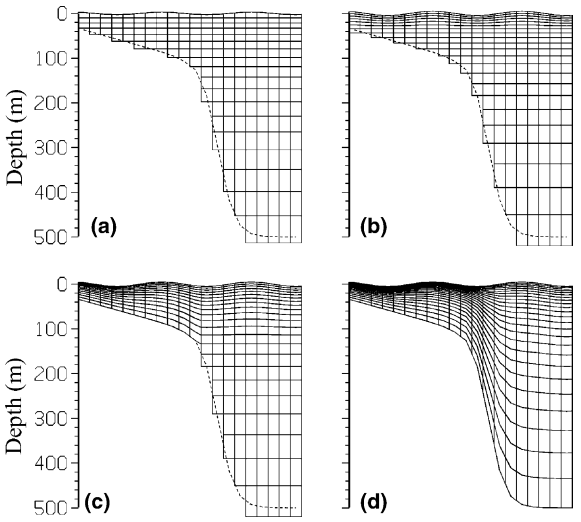

Fig. 1. Schematic illustrations of vertical grid options available in the Navy Coastal Ocean Model (NCOM): (a) a single σ-layer at the surface and z-levels below, (b) several σ-layers near the surface with z-levels below, (c) σ-layers to the bottom over the shelf and above z-levels in deeper water, and (d) σ-layers everywhere. Judicious partitioning between σ- and z-levels can mitigate problems associated with either pure coordinate.

2.3. Finite differencing in NCOM

NCOM uses a staggered Arakawa C-grid with potential temperature (T), salinity (S) and density ρ. The pressure (p) is defined at the center of the grid cells, while the velocity components (u, v, w) are defined at the center of the faces of the grid cells. The eddy coefficients (A_M, A_H, k_M, k_H) are calculated at the staggered grid locations; i.e., at the same locations as the velocities.

NCOM's basic spatial averages and finite differences are mainly second order with some options for higher-order formulations. The spatial differencing of the horizontal pressure gradient term on the σ part of the grid is evaluated as in Blumberg and Mellor (1987). There is an option for the quasi-third order upwind advection scheme described by Holland et al. (1998) for momentum and scalars and an option for the Flux-Corrected Transport (FCT) advection scheme (Zalesak, 1979) for scalars, which avoids advective overshoots. There are also options for fourth-order evaluation of the horizontal pressure gradient (McCalpin, 1994) and fourth-order interpolation of the Coriolis terms. The higher-order formulations are fairly efficient to use except for the FCT advection scheme, which increases the model's running time by 50% or more. Of these higher-order options, only the quasi-third order upwind advection is employed within the cases presented here.

Temporal differencing is leap-frog with an Asselin (1972) filter to suppress timesplitting. All terms are treated explicitly in time except for the solution for the free surface and vertical diffusion. In the solution for the free surface, the surface pressure gradient terms in the depth-averaged momentum equations and the divergence terms in the depth-averaged continuity equation are evenly split between the old and new time levels to minimize the damping of surface waves. In the vertical diffusion terms, the field being diffused is taken to be fully at the new time level to avoid diffusive overshoots and vertical gradient reversals.

The free-surface mode is calculated implicitly; therefore, the surface pressure gradients and the divergence terms in the surface elevation equation have a component at the new time level being calculated.

Horizontal mixing is lagged, i.e., evaluated at $n-1$, which is required for stability. Vertical mixing is fully implicit, so the vertical heat flux is calculated as

$$-K_H^{n-1}\frac{\partial T^{n+1}}{\partial z}. \tag{8}$$

Here the vertical eddy coefficient is evaluated using the values of the model fields at $n-1$, which helps to avoid exciting timesplitting behavior in the leap-frog scheme. Fully implicit vertical mixing is needed to avoid spurious flip-flopping of the vertical gradients, which can occur with a partially implicit scheme when the vertical eddy coefficients become very large in regions of strong vertical mixing. The advection, baroclinic pressure gradient and Coriolis terms are evaluated at the central time level (n). The bottom drag is quadratic, as shown below. Note that to avoid timesplitting, the explicit speed term is calculated at the $n-1$ time step.

$$K_M\frac{\partial u}{\partial z} = c_b u^{n+1}\,|\mathbf{v}^{n-1}|, \tag{9}$$

$$K_M\frac{\partial v}{\partial z} = c_b v^{n+1}\,|\mathbf{v}^{n-1}|\,. \tag{10}$$

2.4. Computational procedures

New baroclinic horizontal velocities are calculated using an estimate of the new surface elevation, and the forcing terms for the baroclinic velocities are vertically integrated to provide the forcing terms needed for the depth-averaged barotropic equations. The depth-averaged momentum and continuity equations are then implicitly solved for the new surface elevation and depth-averaged velocities. The new 3D fields of baroclinic velocities calculated in the previous step are corrected by adding a depth-independent correction so that their vertical mean agrees with the new depth-averaged velocities. This effectively corrects the 3D velocities for the new surface elevation gradient. The velocity field that will be used to advect the scalar fields is calculated by adding a depth-independent correction to the 3D velocity fields at time level n, so that the depth-average of the advection velocities is consistent with the depth-averaged continuity equation. New values of the potential temperature (T and S) are calculated using the previously computed advection fields.

The correction of scalar advection field ensures that the velocity field used to advect the scalars is numerically non-divergent, which avoids spurious sources and sinks when using the flux form of numerical advection. However, in the flux formulation of the advection of momentum, momentum is not strictly conserved without an iterative approach or other modification. The advection of momentum terms are needed to calculate a new elevation, but a new elevation is needed to solve for the momentum advection in a manner that is completely conservative. This is a difficulty for all implicit, free-surface models and also for free-surface models that use a separate, small timestep for the free-surface equations. Iteration of the solution of the baroclinic momentum and depth-averaged equations to eliminate this inconsistency is provided for in the model, with global NCOM configured for a single iteration. More iterations can be used where deemed appropriate, but in tests that have been conducted, the effect of additional iterations to remove the slight inconsistency between the momentum advection and the change in surface elevation was not significant.

Another difficulty in the numerical calculation involves the partially implicit bottom drag term. If the bottom drag is explicit, the implicit vertical mixing and the bottom drag are numerically decoupled from the solution of the depth-averaged equations. However, there is no decoupling when the bottom drag calculation involves the new velocities. The initial, uncorrected estimate of the new baroclinic velocities will be involved in the calculation of the bottom drag, which is part of the forcing term for the barotropic mode. For this reason, it is important that the initial calculation of the baroclinic velocities (i.e., uncorrected for the new surface elevation) be as accurate as possible.

A procedure that is frequently used with σ coordinates, and in the σ portion of NCOM as well, is to subtract the mean horizontal density profile from the density field before calculating the horizontal density gradient (Blumberg and Mellor, 1987), and to subtract a spatially smooth (e.g., climatological or horizontally averaged) temperature and salinity from the temperature and salinity fields when calculating horizontal diffusion of these fields (Mellor and Blumberg, 1985). These fields are calculated from the horizontal averages over the entire domain of the background climatology and vary only with depth. These steps are taken to reduce truncation error when calculating the horizontal density gradient, and to reduce the vertical component of diffusion of temperature and salinity that occurs when horizontal diffusion is calculated along sloping σ

surfaces. These options are used in the global cases here but may be omitted if desired for a particular application.

3. NCOM setup for global simulations

The global NCOM simulations presented in this paper are conducted on a 2048×1280 curvilinear grid, a rotated reprojected bipolar grid with a transition zone (Murray, 1996) extending from 80°S to the full Arctic cap (Fig. 2). From Antarctica to ≈32°N, the grid is spherical with stretching to maintain a grid horizontal aspect ratio near 1 with resolution $\approx 1/6^\circ \times 1/5^\circ \cos\theta$ (longitude × latitude), where θ is latitude. This translates to ≈14 km grid spacing, or ≈1/8° latitude, at 45°S. South of ≈72°S the latitudinal grid spacing remains constant to reduce the number of and computational effort allocated to grid cells around Antarctica. North of ≈32°N the grid enters a transition zone to a bipolar reprojected Arctic cap with ≈47°N singularities over land in Canada and Russia, to minimize the distortion of ocean grid cells. Grid spacing in the Arctic cap is 5–15 km.

The model has a total of 40 vertical material layers (41 interfaces): 19 σ-layers from the surface to 137 m depth and 21 z-levels from 137 m depth to the maximum depth at 5500 m. This configuration would be best depicted by Fig. 1c. The vertical grid is logarithmically stretched so that the open ocean uppermost material level has a rest depth thickness of 1 m. Under this logarithmic stretching, the interface at 137 m is taken as an approximate depth above or near a typical shelf break and thus appropriate for a σ to z transition. NCOM uses realistic bottom

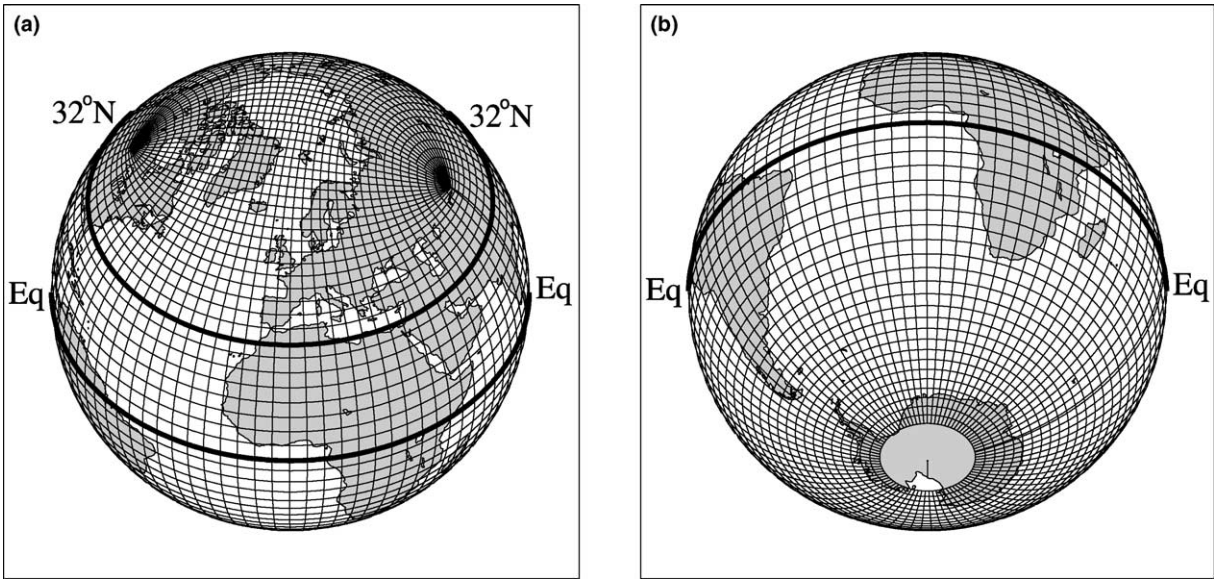

Fig. 2. The curvilinear NCOM grid: (a) northern hemisphere, and (b) southern hemisphere. The transition zone from a stretched spherical grid to a rotated reprojected bipolar grid begins at 32°N.

topography obtained from the 2-min Digital Bathymetric Data Base-Variable resolution (DBDB-V2) data (Ko, 2004, personal communication). This includes all the continental shelves for depths >5 m.

Global simulations on the grid size used by global NCOM require a lot of computer time, so an emphasis of the NCOM design is to maintain a scalable and portable computer code that runs efficiently on different computational architectures. A month-long simulation on the global grid takes approximately 7 h of wall-clock time on 128 processors of the IBM P3 located at NAVOCEANO, Stennis Space Center, MS.

Two global NCOM simulations are performed to examine some of the implications of using different vertical coordinate systems: (1) σ–z (hybrid) and (2) pure z-level. In a rest situation with no elevation anomalies, these coordinate systems match in regions with bottom depth greater than 137 m, where both have a 1 m thickness in the uppermost material level. Both simulations are identical otherwise. A pure σ coordinate case is not considered because our emphasis on the upper ocean leads to a requirement for the uppermost layer thickness to be approximately 1 m for purposes of potential coupling with global atmospheric models. Under such a restriction, the shallow water levels became too thin in the pure σ case, at least using the same time step as the other cases, a requirement for an equitable comparison.

It must be emphasized that simulations discussed in this paper use date-specific atmospheric forcing only, i.e., none of the simulations include any date-specific oceanic data assimilation including SST. Assimilative runs are discussed in a companion paper (Kara et al., this issue). To perform simulations, the 1/8° NCOM is first configured for the two grid specifications (σ–z and pure z), separately. It is then forced with atmospehric variables from the Fleet Numerical Meteorology and Oceanography Center (FNMOC) Navy Operational Global Atmospheric Prediction System (NOGAPS) (Rosmond et al., 2002). Both NCOM simulations are run from 1 January to 31 March in 2000, and they start from the same initial state. Before performing these interannual simulations, the model was first spun-up for a little over six years from a climatological initial state to statistical energy equilibrium with monthly mean wind stress and surface heat fluxes obtained from NOGAPS. The model simulations were then extended interannually using 6 hourly atmospheric wind and thermal forcing from NOGAPS.

The model forcing is calculated from the following time-varying atmospheric fields: wind stress at the sea surface (N m^{-2}), air temperature at 10 m above the sea surface (C), air mixing ratio at 10 m above the sea surface (g kg^{-1}), and net shortwave and net longwave radiation at the sea surface (W m^{-2}). The sensible and latent heat fluxes (W m^{-2}) entering the net surface energy balance equation are strongly dependent on SST and are calculated every time step using the model SST in bulk formulations that include effects of air–sea stability through the exchange coefficients (Kara et al., 2002). The annual climatological SST cycle is built into the model to a limited extent, Including air temperature in the formulations for latent and sensible heat flux along with model SST in the bulk formulation automatically provides a physically realistic tendency towards the correct SST as discussed in another OGCM study by Kara et al. (2003). Although radiation fluxes also depend on SST to some extent, these fluxes are obtained directly from NOGAPS in order to use the atmospheric cloud mask. For these experiments, the shortwave radiation has been filtered to remove the bias caused by 6-h sampling but also eliminating the diurnal heating signal.

4. Evaluation of vertical coordinate system choices

Because all the atmospheric forcing is interannual, the SST predicted by NCOM can be compared with interannual SST obtained from buoy measurements. Daily averaged buoy SSTs are used from three sources: (1) the Tropical Atmosphere-Ocean (TAO) array (McPhaden et al., 1998), (2) the Pilot Research Moored Array (PIRATA) (Servain et al., 1998), and (3) the National Oceanic Data Center (NODC) database (more details available at www.nodc.noaa.gov/BUOY/buoy.html). All the buoys report hourly SST measured at a depth of ≈1 m below the sea surface. For the model-data comparisons, daily-averaged buoy SSTs were formed. The reader is referred to Kara et al. (this issue) for a more detailed information about the buoy data and their use in the model validation. SSTs from NCOM were also extracted at the buoy locations. Since the filtering to minimize sampling bias in the thermal forcing removes the diurnal forcing signal for these comparisons, NCOM in these evaluations does not simulate the diurnal cycle and there is no need to form a daily average of model SST. As mentioned earlier, these are atmospherically-forced free-running simulations; the model assimilates no data used for model-data comparisons nor any other subsurface or SST observations.

We have chosen four buoys to demonstrate, through simulations of daily SST, the impact of using σ–z versus pure z coordinates in the 1/8° NCOM. Three out of four buoys are from NODC, while the other is from the TAO array. The NODC buoys are located near the coastal regions (Table 1), where possible differences between σ–z versus pure z simulations of SST are anticipated to arise. Water depths where these buoys are located are also very shallow (<55 m). In contrast, the TAO buoy in the eastern Equatorial Ocean (08°N, 155°W) is in a location with bottom depth 5249 m. This buoy is included in the analyses to compare σ–z and pure z coordinate systems between coastal (three NODC buoys) and open ocean (a TAO buoy) locations.

The effects of running the model with the pure z coordinate rather than the σ–z coordinate are clearly seen at the three NODC buoys (Fig. 3). The model SST obtained from the pure z simulation tends to be colder than that obtained from the σ–z simulation on most of the days at (40°N, 073°W) and (42°N, 071°W) from 1 January to 31 March 2000. In general, the SST time series from the σ–z simulation follows buoy SST better than that from the pure z simulations at NODC buoys, but there is almost no difference in SST obtained from the pure z simulation versus the σ–z

Table 1
Sample buoy locations from the National Oceanic Data Center (NODC) and Tropical Atmosphere Ocean (TAO) arrays used in the text

Buoy name	Buoy: ID	Buoy location	Latitude–longitude (°)	Depth (m)
Delaware Bay	NODC: 44009	(38°N, 075°W)	38.45°N–074.70°W	28
Long Island	NODC: 44025	(40°N, 073°W)	40.25°N–073.17°W	40
Boston	NODC: 44013	(42°N, 071°W)	42.35°N–070.68°W	55
Equator	TAO: Pacific	(08°N, 155°W)	07.97°N–155.00°W	5249

The list includes buoy name, buoy originator (NODC or TAO), approximate coordinates, for simplicity, as used in the text and more precise latitude and longitude. Water depth where the buoy is located is also given. Daily averages of SST for each buoy are constructed from hourly SST values. The buoy near the mouth of Delaware Bay is roughly 48 km southeast of Cape May, New Jersey, USA, the one near Long Island is about 61 km south of Islip, New York, USA, and the northernmost buoy is almost 30 km east of Boston, Massachusetts, USA.

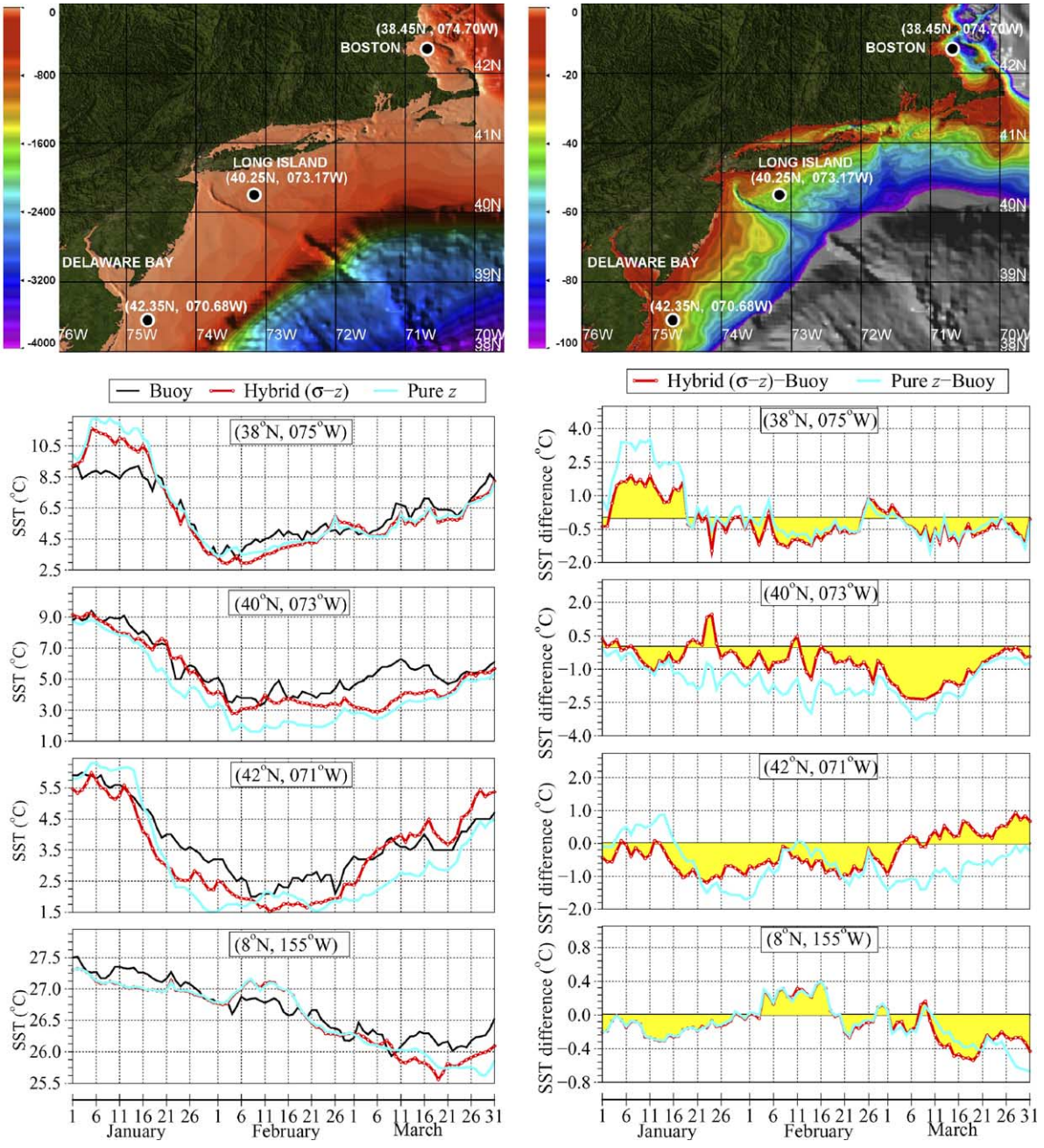

Fig. 3. Bottom topography formed from the 1 min Digital Bathymetric Data Base-Variable (DBDB-V) resolution data set of NAVOCEANO. Two different color bars are used to emphasize different depth ranges: deep water and shallow water (<200 m) (top left and right panels). Daily SST time series obtained from buoys (black), 1/8° NCOM using the σ–z (red), and 1/8° NCOM using the pure z (cyan) coordinates at four locations (three NODC buoys and one TAO buoy) over 1 January 2000–31 March 2000. Also shown are daily SST differences between buoys and 1/8° simulations using the σ–z and pure z coordinates, separately. The reader is referred to the text for detailed buoy specifics. Note that there is no data assimilation in the NCOM simulations.

simulation at the TAO buoy located over the open ocean. As σ–z vertical coordinates designate the shallow depths to be represented by the σ coordinates, the between the pure z and σ–z are usually expected near coastal boundaries at shallow depths.

We further analyze the model results to demonstrate the impact of vertical coordinate choices in the global NCOM simulations. Several statistical metrics are used for comparing the SST time series between buoy and 1/8° NCOM. Let $X_i(i = 1, 2, \ldots, n)$ be the set of n buoy (i.e., reference) values, and let $Y_i(i = 1,2, \ldots, n)$ be the set of corresponding NCOM estimates. Also let $X(Y)$ and $\sigma_X(\sigma_Y)$ be the mean and standard deviations of the reference (estimate) values, respectively. Here, n is 91 days, spanning the 1/8° NCOM simulation performed from 1 January 2000 to 31 March 2000. Following Murphy (1988), the statistical metrics used for model-data comparisons are as follows:

$$\mathrm{ME} = \overline{Y} - \overline{X}, \tag{11}$$

$$\mathrm{RMSD} = \left[\frac{1}{n}\sum_{i=1}^{n}(Y_i - X_i)^2\right]^{1/2}, \tag{12}$$

$$R = \frac{1}{n}\sum_{i=1}^{n}(X_i - \overline{X})(Y_i - \overline{Y})/(\sigma_X\sigma_Y), \tag{13}$$

$$\mathrm{SS} = 1 - \mathrm{RMSD}^2/\sigma_X^2, \tag{14}$$

where ME is the bias or annual mean difference, RMSD is the root-mean-square difference, R is the correlation coefficient, and SS is the skill score (see also Kara et al., this issue).

Table 2 gives statistical model-data comparisons between the 1/8° NCOM and buoy SST time series at the four locations shown in Fig. 3. ME values (i.e., annual mean SST biases) are generally

Table 2
Statistical verification of daily SST time series between buoy and 1/8° NCOM at four locations

Buoy	1/8° NCOM	RMSD (°C)	ME (°C)	σ_{BUOY} (°C)	σ_{NCOM} (°C)	R	SS
(38°N, 075°W)	Hybrid σ–z	1.06	−0.03	1.73	2.49	0.94	0.63
	Pure z	1.29	0.23	1.73	2.66	0.92	0.44
(40°N, 073°W)	Hybrid σ–z	1.15	−0.81	1.69	1.95	0.91	0.54
	Pure z	1.55	−1.34	1.69	2.15	0.95	0.16
(42°N, 071°W)	Hybrid σ–z	0.58	−0.21	1.11	1.35	0.92	0.72
	Pure z	0.88	−0.61	1.11	1.54	0.94	0.36
(08°N, 155°W)	Hybrid σ–z	0.24	−0.11	0.44	0.52	0.91	0.70
	Pure z	0.26	−0.11	0.44	0.53	0.90	0.66

The number of days used in the statistical analysis is 91 (from 1 January 2000 to 31 March 2000). Statistics include root-mean-square difference (RMSD), mean error (ME), standard deviation for buoy (σ_{BUOY}), standard deviation for 1/8° NCOM (σ_{NCOM}), correlation coefficient (R), and skill score (SS). SS values of 1 indicate perfect simulations. Note that all global NCOM simulations ($\sigma - z$ and pure z) herein are atmospherically-forced free-running and therefore include no assimilation of any SST.

small (close to zero) between the model predicted SSTs and buoy SSTs at all locations. This is true whether 1/8° NCOM simulation is performed with the σ–z coordinate or pure z coordinate. While there is no clear systematic bias at all buoy locations, at these locations during three months generally favoring cooling, the model in either configuration tends to have a cold bias. The negative ME values indicate that 1/8° NCOM slightly underestimates SST, i.e., the model SST is slightly cooler than the buoy SST. Examination of RMS SST difference values clearly reveals that 1/8° NCOM with the σ–z coordinate is superior to the pure z coordinate case for predictions of SST, although the deep water station at (8°N, 155 °W) shows almost no difference. The RMSD with respect to buoy increases by 35% (from 1.15 to 1.55 °C) at (40°N, 073 °W), and by 52% (from 0.58 to 0.88 °C) at (42°N, 071°W) when using the pure z instead of σ–z coordinate in the model. While it is interesting to note at these two locations that the R values are smaller for the σ–z simulation in comparison to the pure z simulation, the differences are not statistically significant from each other at the 95% confidence interval. Essentially, the model is able to the capture the phase of SST variability quite well because the R values are high ($>$0.90) at all locations and cases. Thus, for the cases examined here, the use of σ–z instead of pure z coordinates has significant influence on the bias, both of the mean and of the variance, but has limited effect on the correlation.

In addition to RMSD, the non-dimensional SS is also used for model-data comparisons. The reason for considering SS values in examining model performance is that SST biases are taken into account in the RMS differences, but the latter can be small where SS and R are poor because of a small amplitude of seasonal cycle (or SST variations from day to day) at some locations. In addition, SST standard deviation is not the same at each buoy, so a non-dimensional metric (i.e., SS as used here) is useful for making fair comparison of performance among different buoys. It is noted that the model must have SS >0 to have skill, and SS $= 1$ is perfect skill (see also Kara et al., this issue). The model success in predicting daily SST is also evidenced by SS values which are positive. Comparing relative performance using the different coordinate systems, a substantial improvement is noted in the model simulations performed with the σ–z coordinate over those performed with the pure z coordinate. For example, the SS value at (40°N, 073°W) increases more than a factor of three (from 0.16 to 0.54 °C) when 1/8° NCOM was run with the σ–z versus pure z coordinate. The improvement in SS values is evident at all of these locations when using the σ–z coordinate in model simulation. The σ-z coordinate case produces SS above 0.5 at all four buoy locations, while SS in the z coordinate case exceeds 0.5 only once.

Overall performance of 1/8° NCOM simulations using either σ–z or pure z coordinate is examined at all available TAO, NODC and PIRATA buoy locations (Fig. 4). The variety of the buoy locations improves our ability to discern impact of coordinate system choice and determine which provides superior performance in this application. All TAO and PIRATA buoys are fairly distant from coastal regions, mostly equatorial Pacific and Atlantic, as seen from Appendix B. Results using either σ–z or pure z simulations are expected to be similar at these deep-water, open ocean stations. On the other hand, most NODC buoys are near the coastal boundaries (Appendix C) where the σ–z coordinate is expected to provide superior performance. There are a total of 81 buoys during the three-month period: 40 TAO, 38 NODC and 3 PIRATA buoys, located in different regions of the global ocean. A few data voids existing in buoy SST time series are filled using a cubic interpolation in time.

Daily SST time series from each buoy are compared with series obtained from the model simulations. Statistical metrics are calculated over the 3-month period from 1 January 2000 to 31

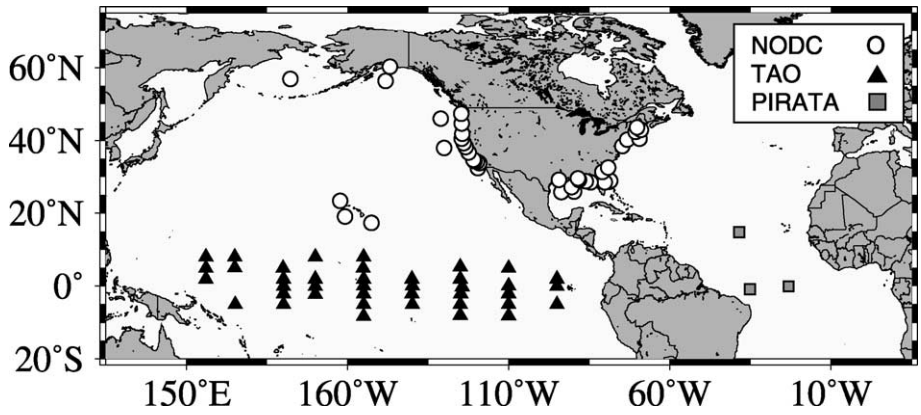

Fig. 4. Locations of NODC, PIRATA and TAO used for model-data comparisons in 2000.

March 2000, similarly to the analyses presented earlier (see Table 2). In particular, the RMSD value is calculated for SST time series between the buoy and 1/8° NCOM using the σ–z coordinate at each NODC buoy location, and the same process is repeated or SST time series between buoy and 1/8° NCOM using the pure z coordinate (Fig. 5). There are clearly large differences in the RMSD at some of the buoy locations, depending the coordinate system used in the model simulation. To better analyze RMS SST difference with respect to daily SST measurements, NODC

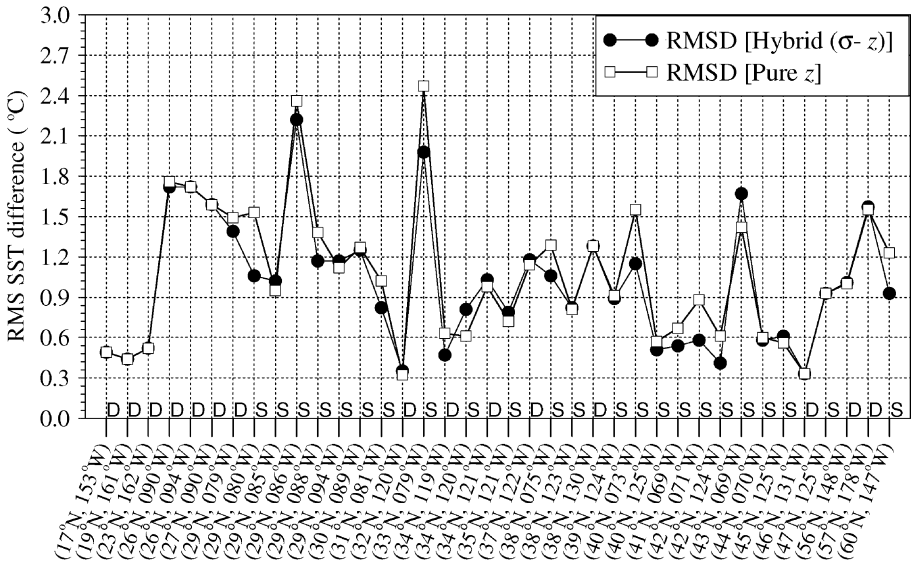

Fig. 5. SST root-mean-square difference (RMSD) between buoy and 1/8° NCOM at NODC buoys over 1 January 2000–31 March 2000. Values are calculated for σ–z and pure z simulations based on the daily SST time series during the 3-month period. In the x-axis, D denotes a buoy located in relatively deep water, while S denotes a buoy in comparatively shallow regions. The model is atmospherically-forced free-running and has no assimilation of any SST or other data. The reader is referred to the text for details of statistical metrics and model simulations.

buoys are separated into two categories as shown in the figure: (1) ones where the depths of water are greater than 400 m (denoted as D), and (2) ones where the depths of water are equal shallower than 400 m (denoted as S). While there are almost no differences in RMS SST differences for buoys located over deep regions, the same is not true for the ones near the coastal regions.

To highlight relative performance in modeling SST, we subtract the RMSD for the z case from the RMSD for the σ–z , where the individual RMSD are relative to the buoy observations as in Fig. 5. Thus a positive difference indicates that the z configuration produced closer agreement with observations than did the σ–z version. The results in Fig. 6 tend negative, indicating superior performance using the σ–z grid. In fact, the RMS SST difference can increase as much as ≈0.5 °C at (29°N, 080°W) and (33°N, 079°W) when using the pure z coordinate as opposed to the σ–z coordinate. While these differences may appear to be small, it should be noted that they correspond to a RMSD increase of 44% (from 1.06 to 1.53 °C) at the former and 25% (from 1.98 to 2.47 °C) at the latter location. RMSD with respect to observations is relatively large even for the σ–z simulation at (33°N, 079°W). A variety of factors beyond the vertical coordinate may be impacting the model performance, and the impact of these may be relatively insensitive to coordinate choice. NCOM suffers from atmospheric forcing that contains errors due to land contamination near the coastal regions, as in other OGCM studies (e.g., Kara et al., 2005); this would primarily be reflected in comparisons with NODC buoys. The atmospheric fields used in the model simulations, NOGAPS in this case, is on a 1° grid, but NCOM is on a much finer grid with resolution near 1/8°. Interpolation of atmospheric forcing fields from NOGAPS to the model grid usually results in errors, especially near the coastal boundaries, as in (33°N, 079°W) because the 1° grid

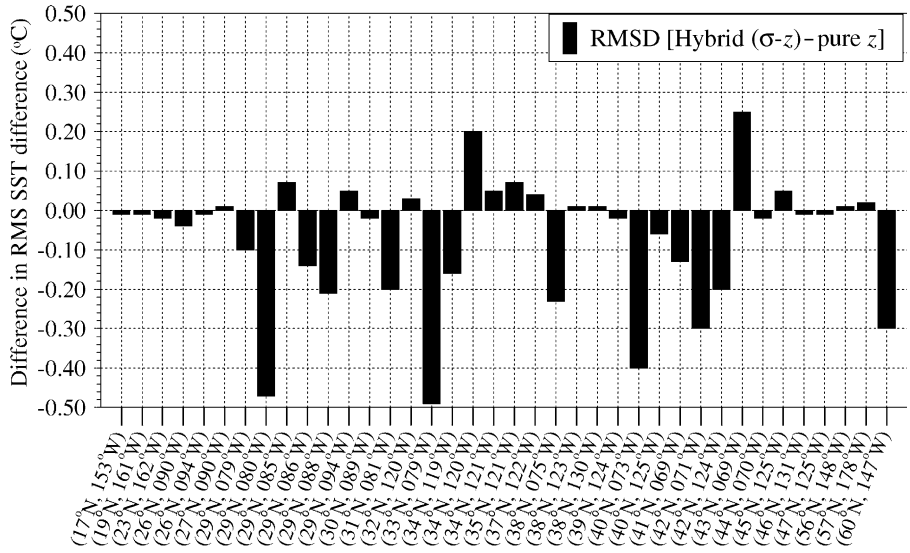

Fig. 6. The difference in RMSD values shown in Fig. 5. It should be noted that the RMSD with respect to the buoy is first obtained for each simulation, separately, and then subtracted from each other. In other words, in the figure legend, RMSD [Hybrid(σ–z)–pure z] represents the RMSD with respect to the buoy for the pure z simulation subtracted from the for the σ–z simulation. There are a total of 24 out of 38 NODC buoys where the the RMS SST difference values for the pure z simulation are larger than those for the σ–z simulation.

from NOGAPS cannot distinguish a precise transition between land and sea, significant for heat fluxes, for example. Further details of this problem are beyond the scope of this paper.

Unlike the RMS SST difference, the R values between the NODC buoy and 1/8° NCOM SST time series are generally similar to each other for σ–z and pure z simulations (Fig. 7) with the exception of a few locations. Overall, the R values obtained from the σ–z simulation are higher than those from the pure z simulation. There are only 11 out of 38 NODC buoys for which the R values from the σ–z simulation ($\approx$1/4 of the buoys) are lower than those from the pure z simulation (Fig. 8). The maximum difference in R, 0.14, is noted at 37°N, 122°W. While the R is 0.55 for the pure z simulation, it improves to 0.69 for the σ–z simulation. The latter R value is statistically significant in comparison to a R value of 0.6, while the former is not.

Finally, we examine how the model simulations with σ–z and pure z coordinates perform for predictions of SST over the open ocean. Such an investigation can be made using TAO and PIRATA buoys located in the equatorial Pacific and Atlantic Ocean, where the depth of water is >4000 m at most observation sites. Unlike the NODC buoys, the differences in RMS SST difference for these locations do not indicate that the simulation using the σ–z is superior, in terms of SST simulation, to the case using the pure z coordinate (Fig. 9). There are 18 out of 40 TAO buoys where the RMS SST difference with respect to the buoy from the σ–z simulation is lower than the one from the pure z simulation. Thus, 1/8° NCOM performs relatively well at approximately half of the buoy locations when using the σ–z simulation, while use of the pure z coordinate has better success at the other buoy locations.

Essentially, one must note that the differences in RMS SST difference at the TAO locations are much smaller than those at the NODC locations (see Fig. 6). They are generally close to zero and always within the small range of −0.2 to 0.2 °C. Such RMS SST difference values confirm the fact

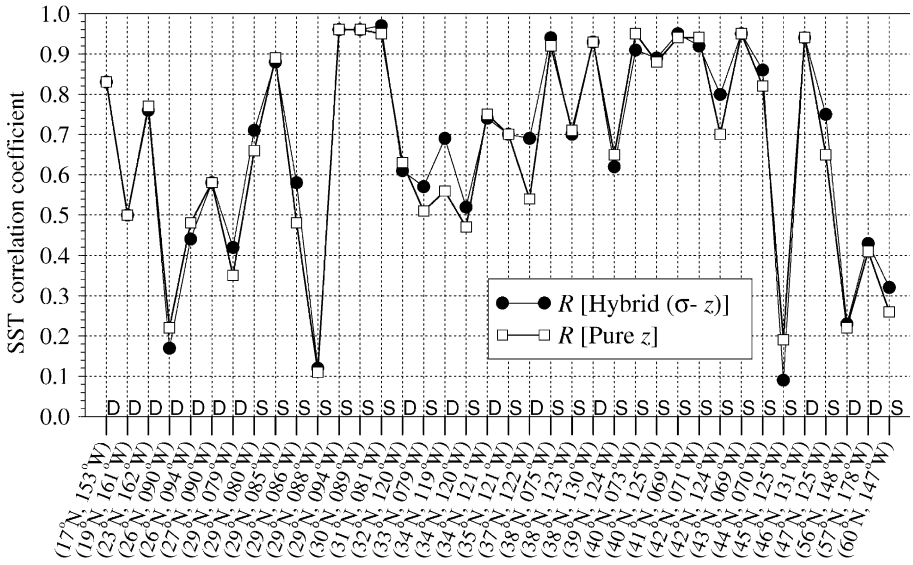

Fig. 7. The correlation coefficients (R) are between the NODC buoy observations and 1/8° NCOM SST time series over 1 January 2000–31 March 2000, shown separately for the σ–z and pure z simulations. Below the x-axis, D denotes a buoy located in deep water, and S denotes a buoy near the shallow regions.

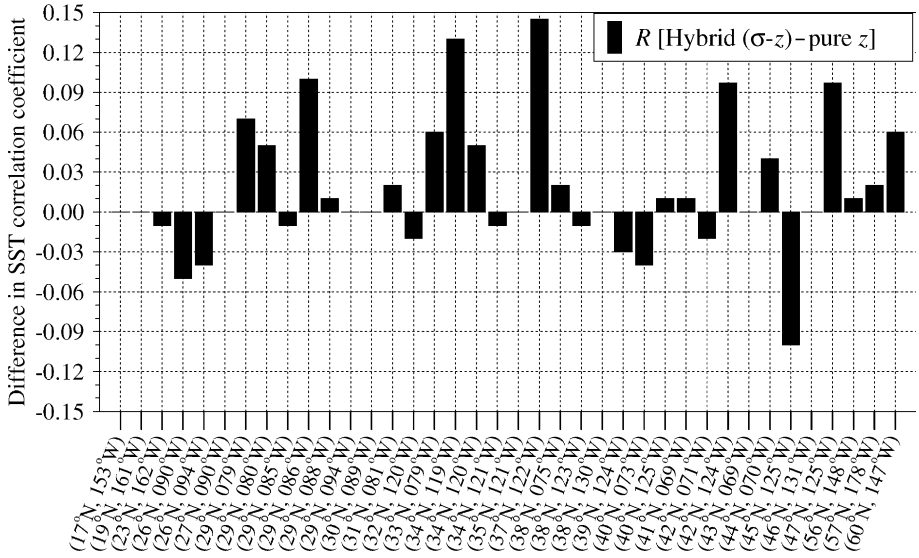

Fig. 8. The difference in R values shown in Fig. 7. In the figure legend, R [Hybrid(σ–z)–pure z] represents the R with respect to the buoy for the pure z simulation subtracted from the R for the σ–z simulation. There are a total of 11 out of 38 NODC buoys where the the SST correlation coefficient for the pure z simulation is higher than the correlation coefficient for the σ–z simulation.

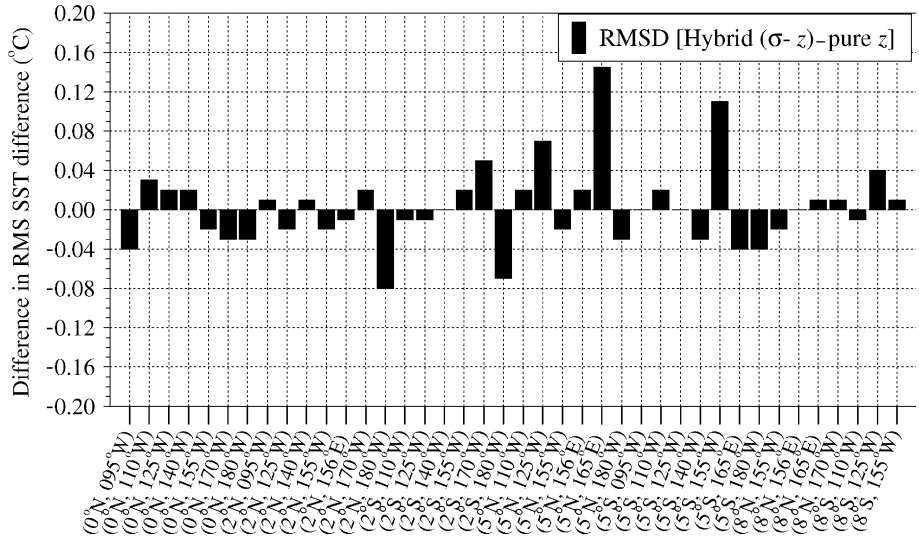

Fig. 9. The difference in RMSD values at TAO buoys. In the figure legend, RMSD [Hybrid(σ–z)–pure z] represents the RMSD with respect to the buoy for the pure z simulation subtracted from the for the σ–z simulation. There are a total of 22 out of 40 TAO buoys where the the RMS SST difference values for the pure z simulation are lower than those for the σ–z simulation.

that in the open ocean, there is not a clear advantage of the σ–z coordinate over the pure z coordinate. Similar to the differences in RMS SST difference, we note that the R values do not differ

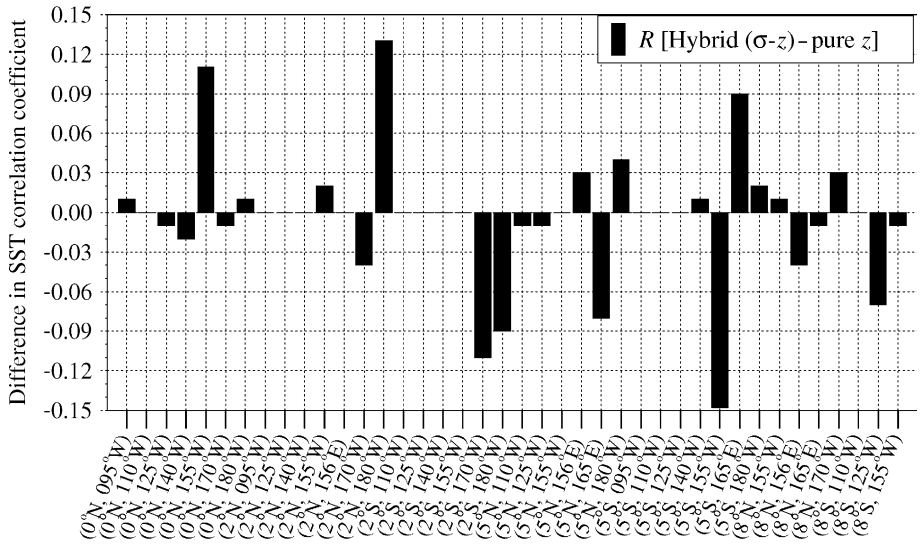

Fig. 10. The difference in R values at TAO buoys. In the figure legend, R [Hybrid(σ–z)–pure z] represents the R with respect to the buoy for the pure z simulation subtracted from the R for the σ–z simulation. There are a total of 14 out of 40 TAO buoys where the the SST correlation coefficient for the pure z simulation are higher than those for the σ–z simulation.

significantly from each other when using either coordinate configuration at the TAO buoy locations (Fig. 10). The R values with respect to buoy from the σ–z simulation are higher than those from the pure z simulation at 65% (26 out of 40) of the TAO buoy locations as implied by the differences in SST correlation coefficient. On the other hand, some of the R values from both simulations are not statistically different from a correlation coefficient of 0.6, and differences in most of the R values are usually very small (<0.05), resulting in a conclusion that the coordinate differences do not have a significant effect in deep water on the shape of the daily SST time series. The magnitude of the R value differences exceeds 0.1 only at four TAO buoys. The model SST results were also analyzed at 3 PIRATA buoys, (0°N, 023°W), (0°N, 035°W) and (15°N, 038°W), where the SST time series were available over 1 January 2000–31 March 2000. There were almost no differences between the statistical results for these locations using the σ–z coordinate as opposed to the pure z coordinate in the model simulations (not shown), fn fact, the SST time series were identical from both simulations at (0°N, 035°W).

5. Impact of coordinate system choice on subsurface temperatures

Following the discussions presented in the earlier section, we now examine how the choice of vertical coordinate system (σ–z or pure z) affects subsurface temperatures. Fig. 11 shows cross-sections of subsurface temperatures obtained from model simulations performed with σ–z and pure z coordinates at 40.25°NN. This latitude for the cross-section analysis is chosen because there are large differences in SS values at (40°N, 073°W), as presented earlier.

Differences are evident in a comparison of the mean sections. One stark difference is in the development of cold core along the coast, which is evident in the σ–z simulation but much stronger, on

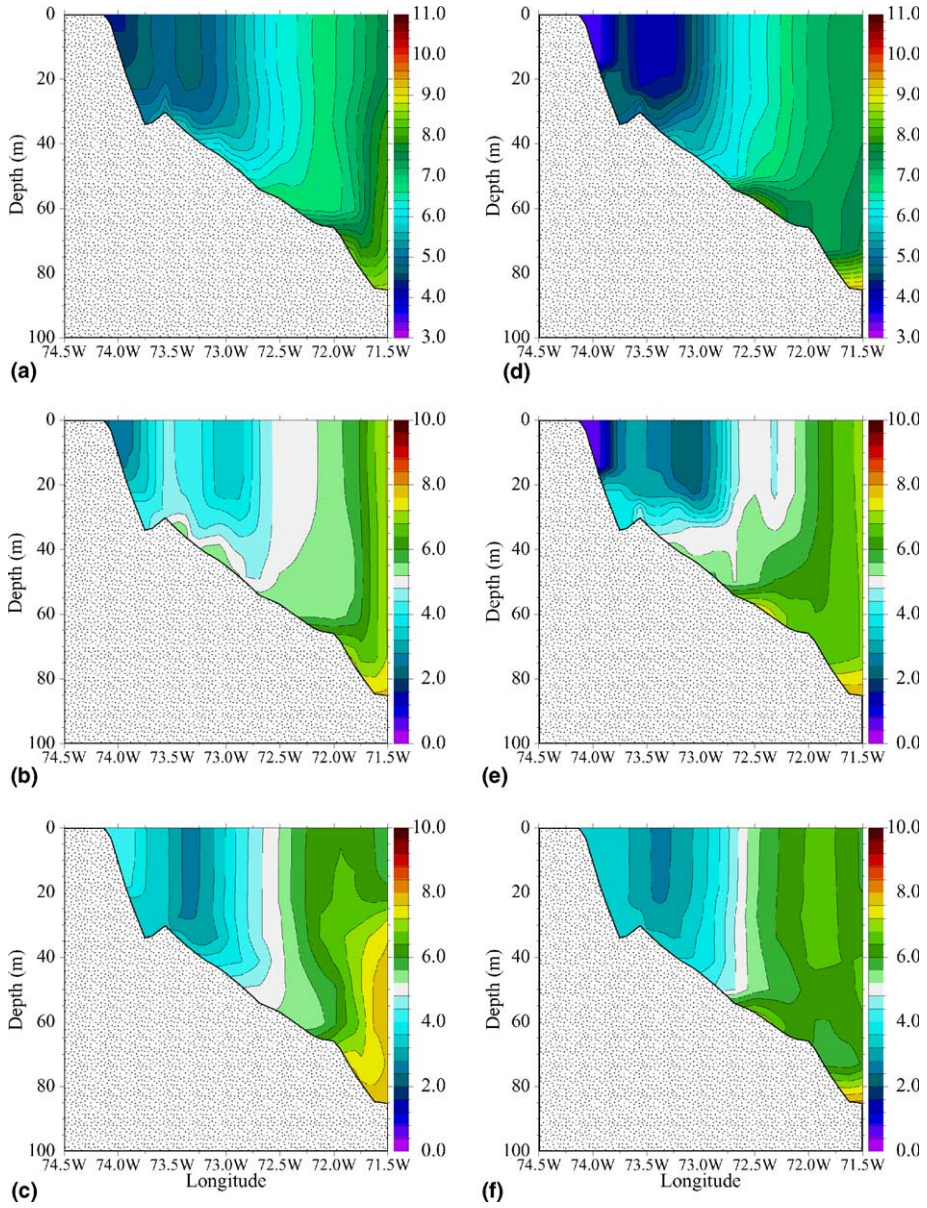

Fig. 11. Comparisons of vertical temperature sections off the eastern coast of the United States at 40.25°N. The σ–z and pure z simulations show significant differences, with the σ–z showing better agreement with a time-series of buoy SST observation (Fig. 3). For plotting purposes, a dotted land mask is superimposed on filled temperature fields; it does not reflect the discrete steps of the z-level bathymetry that contribute to some of the differences. (a) σ–z simulation: January–March 2000 mean, (b) σ–z simulation on 11 February 2000, (c) σ–z simulation on 3 March 2000, (d) pure z simulation: January–March 2000 mean, (e) pure z simulation on 11 February 2000, (f) pure z simulation on 3 March 2000.

the order of 1 °C colder, in the z case. Comparison of SST at (40°N, 073°W) in Fig. 3 shows a cold bias in the z simulation, suggesting that the cold core in z is too strong and better represented by

the σ–z configuration. Higher vertical resolution in the hybrid coordinate version may play a role in its relatively better performance; for the depths shallower than 40 m in this zone, the σ–z grid has 19 levels while the pure z version is limited to no more than 12 levels. The z grid also shows some evidence of warm patches along the bottom that may be a result of the truncated bathymetry. The z case mean contains stronger horizontal gradients of temperature inshore, reflecting the stronger cold filament along the coast, while the σ–z simulation has stronger horizontal gradients near the 100 m isobath.

Because subsurface temperature time series are not available from NODC buoys, where the largest SST differences are seen between the σ–z or pure z simulations, SST is used to guide expectations regarding the accuracy of subsurface temperatures in the cross-section analysis. Two specific days are considered: 11 February 2000 and 3 March 2000. As indicated by Fig. 3, the largest SST difference during the 3-month period at (40°N, 073°W) occurs on 11 February 2000. On this day, the SST from the σ–z simulation agrees closely with the observation, while the z case shows a significant cold bias. We take this to imply that subsurface temperatures along this section on 11 February 2000 are likely better represented by the σ–z simulation than by the pure z. This comparison is additional evidence that the z configuration overestimates the size and strength of the cold core along the coast. At the other extreme, the largest errors during the 3-month period at this location occur in early to mid March. On 3 March 2000 the models are in fairly close agreement with each other but are significantly colder than the observation, by ≈1.8 °C for the σ–z simulation and ≈2.3 °C for the pure z case. Since the model SST difference is comparatively small on this date, we anticipate that subsurface temperatures at (40°N, 073°W) should be similar, at least up to some extent near the sea surface. This is the case inshore, but differences are present at depth along the 100 m isobath. The σ–z simulation is approximately 2 °C warmer. Information beyond SST is required to determine which case is closer to actual conditions.

Observations of vertical temperature profiles provide additional insight into the impact of vertical coordinate choice on subsurface temperature. Temperature profile data are obtained from the Marine Environmental Data Service (MEDS) at three locations available during 1 January 2000–31 March 2000. MEDS acquires, processes, quality controls and archives real-time drifting buoy messages reporting over the Global Telecommunications System (GTS) as well as delayed mode data acquired from other sources. Further information about the MEDS data sets is available at www.meds-sdmm.dfo-mpo.gc.ca/meds/Databases/Data_e.htm.

Comparisons of subsurface temperatures from NCOM and MEDS are made at three locations (Fig. 12). One (43.9°N, 63.7°W) is in the western North Atlantic near the shelf break, ≈200 m depth off the coast of Nova Scotia. The second (40.6°N, 130.1°W) is in the Japan/East Sea (JES), not far from the coast but in fairly deep water (≈2300 m), and the third is in the deep, open ocean of the central North Pacific (31.6°N, 173.20°W, ≈5000 m depth). These samples reflect shelf edge, semi-enclosed sea and open ocean regions. Temperature profiles at these locations are compared on 5 February 2000, 15 March 2000 and 16 February 2000, respectively. Subsurface temperatures from the NCOM models are extracted for the same dates and locations. A linear interpolation is applied to NCOM data to match depths levels of the MEDS profiles, allowing profiles to be compared at the same depths.

For these cases, the σ–z solutions are preferable to those from the pure z simulation. Solutions are generally similar below 200 m, a zone where the coordinate systems match. Above 200 m, the σ–z results tend to be in closer agreement with the observations. An exception is the JES

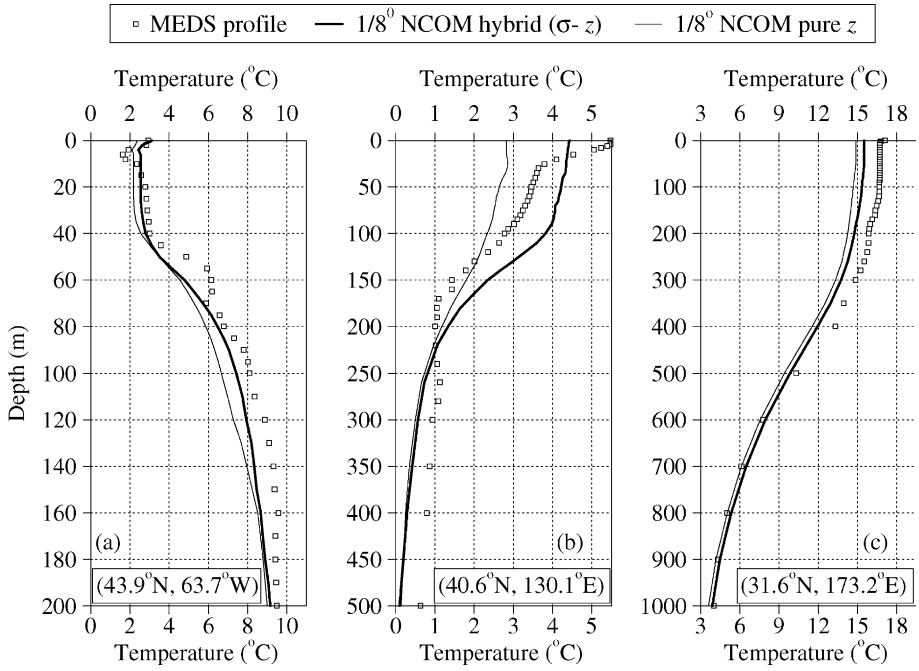

Fig. 12. Comparisons of temperature profiles between 1/8°NCOM and MEDS data at three locations: (left) Shelf edge off Nova Scotia, 43.9°N, 63.7°W, ~200 m depth, 5 February 2000; (center) Japan/East Sea, 40.6°N, 130.1°W, ~2300 m depth, 15 March 2000; (right) central North Pacific, 31.6°N, 173.20°W, ~5000 m depth, 16 February 2000.

observation, where the z simulation has smaller temperature errors between 100 and 200 m. However the shape and associated temperature gradients, more important than actual temperature for acoustic applications, are generally better from the σ–z simulation. Neither model reproduces some of the finer scale details, such as the warm layer in the upper 25 m in the JES sample and the temperature inversion at a depth of 70 m in the profile near Nova Scotia. Details at this scale would likely require assimilative runs at higher resolution for more realistic representation. Differences are small in the open ocean case, as expected.

6. Discussion and conclusions

We have described the configuration and global implementation of 1/8° global NCOM. The model is baroclinic, hydrostatic, Boussinesq, and has a free-surface. It uses curvilinear coordinates in the horizontal, configured with a rotated reprojected bipolar grid in the Arctic. One of its distinguishing characteristics is the σ–z coordinate in the vertical, combining z-levels for depths above a user-specified depth, here 137 m, with z levels below. The use of combined σ and z-level coordinates in a single model provides some flexibility in setting up the vertical grid to address problems that are expected using more traditional vertical coordinates.

A pair of atmospherically-forced free-running simulations conducted with the model using either σ–z or z-level vertical coordinates demonstrate the flexibility of the model and illustrate

some consequences arising from the coordinate choices. It is noted that in NCOM z-level coordinates the bathymetry is rounded to the nearest model level, so simulations have a sub-optimal representation of changes in the bottom depth. The model solution obtained is for the stair-step bottom used in the model, rather than the actual bathymetry. Onshore and offshore barotropic flows can be noticeably distorted by the stairsteps of a z-level grid. While σ coordinates accurately represent the changing bottom depth, they can suffer from problems with their horizontal advection, diffusion, and baroclinic pressure gradient terms in regions of steep bottom slopes. Large changes in depth between adjacent grid points can result in large changes in the model fields between grid points in the near-bottom σ layers due to large vertical gradients in the oceanic fields. This can present problems for numerical advection schemes that require gradients to be resolved by a number of points for accuracy. Horizontal diffusion between adjacent grid points that are at significantly different depths can effectively result in vertical diffusion of model fields, which is generally outside of turbulent boundary layers where oceanic vertical diffusion tends to be small.

A number of solutions could be proposed to mitigate shortcomings of various vertical coordinate approaches. One solution to these types of truncation error problems is to increase grid resolution. However, due to limited computing resources, this is not always practical. The impact of the cost of more expensive numerical methods is particularly felt in global scale operational models limited by operational time and resource constraints. A detailed examination of a wide range of mitigation techniques and coordinate definitions is beyond the scope of this paper. We merely present the approach used in global NCOM, the hybrid σ–z coordinate, and compare samples of its results with a parallel case using a more-traditional z coordinate. The combined σ–z grid allows the use of multiple σ coordinates near the surface to take up changes in surface elevation. This appears to be more robust at longer time steps than a single free surface. In shallow water, where flow is expected to be more sensitive to accurate representation of bottom depth, the σ coordinates allow fidelity to bottom topography and more consistent resolution in the bottom boundary layer. z-levels can be used in the deeper water, e.g., below the continental shelves where the bottom slopes can be very steep, to avoid some of the problems associated with σ coordinates over steep topography. The global simulations conducted with both σ–z and z-level coordinates to assess the extent of differences caused by the different coordinate systems show greatest impact in nearshore regions and small impact in open ocean regions, as expected. For global NCOM, comparisons with temperature observations indicate improved overall performance using the σ–z coordinates relative to pure z coordinates.

Operational global NCOM provides the US Navy a readily available first look at mesoscale circulation conditions in any region of the global ocean. A perhaps more important objective is to provide initial and boundary conditions for fixed and relocatable ocean models. Some regional applications have been tested in the North Atlantic, East Asian Seas, Intra-Americas Seas, Gulf of Mexico, and US west coast regions. Analyses of these applications will be reported in future articles. Further objectives of global NCOM include providing capability as the ocean model component for a global, coupled, air-ocean modeling system and hosting an embedded Arctic ice model. NCOM has been specifically developed to be suitable for coupling in a regional air/ocean system, making global NCOM a candidate for use as the ocean component in a global coupled system. Work on embedding the Polar Ice Prediction System (PIPS) 3.0, the latest generation of the Navy ice model, is scheduled to begin in late 2004. Work continues on refinements to the model implementation and data assimilation. Additional results and information may be found at

the global NCOM web page, www.ocean.nrlssc.navy.mil/global_ncom. An evaluation of the baseline model capability is necessary to complement specialized assessment of specific applications. Capabilities of NCOM over the global ocean are examined in Kara et al. (this issue), in detail.

Acknowledgement

The authors would like to thank Dong Ko and P. Flynn of the Naval Research Laboratory (NRL) for their work in creating the model grid and bottom topography map. Appreciation is extended to the National Data Buoy Center (NDBC) and M. McPhaden of the Tropical Ocean Array (TAO) project office for making daily SST and subsurface temperature data available. Special thanks go to two anonymous reviewers whose constructive suggestions and criticisms certainly improved quality of this paper. Contributions to this work were funded as part of the NRL 6.4 Large-scale Models, 6.4 Ocean Data Assimilation, and 6.4 Small Scale Oceanography projects, managed by PMW180 under program element 0603207N. This work received additional funding from the 6.1 Dynamics of Low latitude Western Boundary Currents project funded by the Office of Naval Research (ONR) under program element 601153N. The numerical simulations were performed under the Department of Defense High Performance Computing Modernization Program on an IBM SP3 at the Naval Oceanographic Office, Stennis Space Center, Mississippi. This is contribution NRL/JA/7320/03/105 and has been approved for public release.

Appendix A. A list of symbols

A_H	horizontal mixing coefficient for temperature or salinity ($m^2\ s^{-1}$)
A_{H_0}	constant background value for A_H ($10\ m^2\ s^{-1}$)
A_M	horizontal mixing coefficient for momentum ($m^2\ s^{-1}$)
A_{M_0}	constant background value for A_M ($10\ m^2\ s^{-1}$)
c_b	bottom drag coefficient
f	Coriolis parameter (s^{-1})
g	gravity acceleration ($9.8\ m\ s^{-2}$)
H	the bottom depth (m)
$\hat{\mathbf{i}}$	unit vector in zonal direction
$\hat{\mathbf{j}}$	unit vector in meridional direction
$\hat{\mathbf{k}}$	unit vector in vertical direction
K_H	the vertical eddy coefficient for temperature or salinity ($m^2\ s^{-1}$)
K_M	the vertical eddy coefficient for momentum ($m^2\ s^{-1}$)
p	pressure (mb)
Q_r	net solar radiation ($W\ m^{-2}$)
S	salinity (psu)
u	zonal velocity component ($m\ s^{-1}$)
$\bar{u}$	depth-averaged zonal velocity ($m\ s^{-1}$)
v	meridional velocity component ($m\ s^{-1}$)
$\mathbf{v}$	velocity vector

$\bar{v}$ depth-averaged meridional velocity ($m\ s^{-1}$)
t time (s)
T potential temperature (°C)
x distance in zonal direction (m)
w vertical velocity component ($m\ s^{-1}$)
y distance in meridional direction (m)
z distance in vertical direction (m)
z_b distance to the bottom of the turbulent layer (m)
z_s depth at which the grid changes from σ to z-level (m)
z_t distance to the top of the turbulent layer (m)
γ a function describing the solar extinction
k von Kármán constant (0.4)
∇ Laplacian operator
∇_H horizontal Laplacian operator
ρ water density ($kg\ m^{-3}$)
ρ_0 reference water density (1025 $kg\ m^{-3}$)
σ coordinate transformation (0 to -1)
θ latitude (°)
ζ free surface elevation above the undisturbed value at $z = 0$ (m)

Appendix B. TAO buoy locations

A list of TAO and PIRATA buoys which contain daily-averaged SST data used for NCOM SST intercomparisons in 2000. Water depths at buoy locations are also given. It should be noted that daily averages are constructed from hourly SST values. Since each mooring moves in time and space from its deployment position, we calculated average position based on the historical latitude and longitude data for each buoy. For ease of notation, nearest integer values of average latitude and longitude is used for each buoy.

TAO	Location	(Lat, Lon)	Depth (m)
Pacific	(0°N, 095°W)	(0.01°N, 094.98°W)	3318
Pacific	(0°N, 110°W)	(0.05°N, 109.94°W)	3935
Pacific	(0°N, 125°W)	(0.20°S, 124.36°W)	4780
Pacific	(0°N, 140°W)	(0.05°N, 139.88°W)	4359
Pacific	(0°N, 155°W)	(0.05°N, 154.98°W)	4647
Pacific	(0°N, 170°W)	(0.04°S, 170.02°W)	5616
Pacific	(0°N, 180°W)	(0.02°N, 179.90°W)	5439
North	(2°N, 095°W)	(1.98°N, 095.03°W)	3113
North	(2°N, 125°W)	(1.97°N, 125.07°W)	4745
North	(2°N, 140°W)	(2.01°N, 140.00°W)	4387

(*continued on next page*)

Appendix B (*continued*)

TAO	Location	(Lat, Lon)	Depth (m)
North	(2°N, 155°W)	(2.00°N, 154.97°W)	4661
North	(2°N, 156°E)	(2.00°N, 156.02°E)	2594
North	(2°N, 170°W)	(2.00°N, 170.03°W)	5408
North	(2°N, 180°W)	(2.02°N, 179.80°W)	5477
South	(2°S, 110°W)	(2.00°S, 109.98°W)	3950
South	(2°S, 125°W)	(2.04°S, 124.90°W)	4751
South	(2°S, 140°W)	(2.02°S, 139.95°W)	4320
South	(2°S, 155°W)	(1.99°S, 154.96°W)	4988
South	(2°S, 170°W)	(2.17°S, 170.04°W)	4983
South	(2°S, 180°W)	(2.01°S, 179.90°W)	5353
North	(5°N, 110°W)	(4.94°N, 109.99°W)	3991
North	(5°N, 125°W)	(5.32°N, 124.94°W)	4395
North	(5°N, 155°W)	(4.95°N, 155.09°W)	4597
North	(5°N, 156°E)	(4.99°N, 156.06°E)	3607
North	(5°N, 165°E)	(5.05°N, 164.98°E)	4780
North	(5°N, 180°W)	(4.99°N, 179.93°W)	5680
South	(5°S, 095°W)	(5.02°S, 095.07°W)	3831
South	(5°S, 110°W)	(5.00°S, 109.99°W)	3605
South	(5°S, 125°W)	(5.02°S, 124.95°W)	4561
South	(5°S, 140°W)	(5.01°S, 139.90°W)	4359
South	(5°S, 155°W)	(4.99°S, 154.98°W)	5014
South	(5°S, 165°E)	(5.00°S, 165.20°E)	5418
South	(5°S, 180°W)	(4.98°S, 179.90°W)	5664
North	(8°N, 155°W)	(7.97°N, 155.00°W)	5249
North	(8°N, 156°E)	(7.97°N, 156.03°E)	4920
North	(8°N, 165°E)	(7.98°N, 165.06°E)	5210
North	(8°N, 170°W)	(8.01°N, 170.02°W)	5553
South	(8°S, 110°W)	(8.05°S, 109.93°W)	3465
South	(8°S, 125°W)	(7.96°S, 125.02°W)	4564
South	(8°S, 155°W)	(8.26°S, 155.02°W)	5341
Atlantic	(0°N, 023°W)	(0.02°N, 23.12°W)	3843
Atlantic	(0°N, 035°W)	(0.37°S, 35.06°W)	4421
North	(15°N, 038°W)	(14.94°N, 38.39°W)	5382

Appendix C. NODC buoy locations

The same as Appendix B but for the NODC buoys. The 5-digit numbers column represents buoy ID numbers used by NODC.

NODC	Location	(Lat, Lon)	Depth (m)
51004	(17N, 153°W)	(17.43N, 152.52°W)	5303
51003	(19N, 161°W)	(19.17N, 160.72°W)	4943
51001	(23N, 162°W)	(23.40N, 162.25°W)	3257
42001	(26N, 090°W)	(25.92N, 089.67°W)	3246
42002	(26N, 094°W)	(25.88N, 093.57°W)	3200
42041	(27N, 090°W)	(27.22N, 090.43°W)	1435
41010	(29N, 079°W)	(28.88N, 078.52°W)	841
41009	(29N, 080°W)	(28.50N, 080.18°W)	42
42036	(29N, 085°W)	(28.50N, 084.50°W)	53
42039	(29N, 086°W)	(28.78N, 086.03°W)	283
42040	(29N, 088°W)	(29.20N, 088.20°W)	237
42035	(29N, 094°W)	(29.23N, 094.40°W)	15
42053	(30N, 089°W)	(29.55N, 088.50°W)	40
41008	(31N, 081°W)	(31.40N, 080.87°W)	18
46047	(32N, 120°W)	(32.43N, 119.52°W)	1393
41004	(33N, 079°W)	(32.50N, 079.10°W)	36
46025	(34N, 119°W)	(33.73N, 119.08°W)	859
46053	(34N, 120°W)	(34.23N, 119.83°W)	417
46063	(34N, 121°W)	(34.25N, 120.65°W)	598
46023	(35N, 121°W)	(34.70N, 120.97°W)	384
46042	(37N, 122°W)	(36.75N, 122.42°W)	1920
44009	(38N, 075°W)	(38.45N, 074.70°W)	28
46013	(38N, 123°W)	(38.22N, 123.32°W)	122
46059	(38N, 130°W)	(37.98N, 129.98°W)	4599
46014	(39N, 124°W)	(39.22N, 123.95°W)	264
44025	(40N, 073°W)	(40.25N, 073.17°W)	40
46030	(40N, 125°W)	(40.42N, 124.52°W)	82
44008	(41N, 069°W)	(40.50N, 069.42°W)	62
44013	(42N, 071°W)	(42.35N, 070.68°W)	55
46027	(42N, 124°W)	(41.85N, 124.37°W)	47
44005	(43N, 069°W)	(42.88N, 068.93°W)	21
44007	(44N, 070°W)	(43.52N, 070.13°W)	18
46050	(45N, 125°W)	(44.62N, 124.52°W)	130
46005	(46N, 131°W)	(46.05N, 131.02°W)	2779
46041	(47N, 125°W)	(47.33N, 124.75°W)	132
46001	(56N, 148°W)	(56.28N, 148.17°W)	4206
46035	(57N, 178°W)	(56.90N, 177.80°W)	3662
46061	(60N, 147°W)	(60.20N, 146.83°W)	204

References

Asselin, R., 1972. Frequency filter for time integrations. Mon. Wea. Rev. 100, 487–490.

Barron, C.N., Kara, A.B., Hurlburt, H.E., Rowley, C., Smedstad, L.F., 2004. Sea surface height predictions from the Global Navy Coastal Ocean Model (NCOM) during 1998–2001. J. Atmos. Oceanic Technol. 21, 1876–1894.

Bleck, R., 2002. An oceanic general circulation model framed in hybrid isopycnic-cartesian coordinates. Ocean Modell. 4, 55–88.

Bleck, R., Rooth, C., Hu, D., Smith, L.T., 1992. Salinity-driven thermocline transients in a wind- and thermohaline-forced isopycnic coordinate model of the North Atlantic. J. Phys. Oceanogr. 22, 1486–1505.

Blumberg, A.F., Herring, H., 1987. Circulation modelling using orthogonal curvilinear coordinates. In: Nihoul, J., Jamart, B. (Eds.), Three-dimensional Models of Marine and Estuarine Dynamics. Elsevier Oceanography Series, vol. 45, pp. 55–88.

Blumberg, A.F., Mellor, G.L., 1983. Diagnostic and prognostic numerical circulation studies of the South Atlantic Bight. J. Geophys. Res. 88, 4579–4592.

Blumberg, A.F., Mellor, G.L., 1987. A description of a three-dimensional coastal ocean circulation model. In: Heaps, N. (Ed.), Three-dimensional Coastal Ocean Models. Amer. Geophys. Union, New York, p. 208.

Chassignet, E.P., Smith, L.T., Halliwell, G.R., Bleck, R., 2003. North Atlantic simulation with the HYbrid Coordinate Ocean Model (HYCOM): Impact of the vertical coordinate choice, reference density, and thermobaricity. J. Phys. Oceanogr. 33, 2504–2526.

Craig, P.D., Banner, M.L., 1994. Modeling wave-induced turbulence in the ocean surface layer. J. Phys. Oceanogr. 24, 2546–2559.

Deleersnijder, E., Beckers, J., 1992. On the use of the sigma-coordinate system in regions of large bathymetric variations. J. Mar. Syst. 3, 381–390.

Ezer, T., Arango, H., Shchepetkin, A.F., 2002. Developments in terrain-following ocean models: intercomparisons of numerical aspects. Ocean Modell. 4, 249–267.

Friedrich, H., Levitus, S., 1972. An approximation to the equation of state for sea water, suitable for numerical ocean models. J. Phys. Oceanogr. 2, 514–517.

Halliwell Jr., G.R., 2004. Evaluation of vertical coordinate and vertical mixing algorithms in the HYbrid Coordinate Ocean Model (HYCOM). Ocean Modell. 7, 285–322.

Holland, W.R., Chow, J.C., Bryan, F.O., 1998. Application of a third-order upwind scheme in the NCAR ocean model. J. Climate 11, 1487–1493.

Hurlburt, H.E., Thompson, J.D., 1980. A numerical study of Loop Current intrusions and eddy shedding. J. Phys. Oceanogr. 10, 1611–1651.

Kara, A.B., Barron, C.N., Martin, P.J., Smedstad, L.F., and Rhodes, R.C., this issue. Validation of interannual simulations from the 1/8° global Navy Coastal Ocean Model (NCOM). Ocean Modelling.

Kara, A.B., Wallcraft, A.J., Hurlburt, H.E., 2005. Sea surface temperature sensitivity to water turbidity from simulations of the turbid Black Sea using HYCOM. J. Phys. Oceanogr. 35, 33–54.

Kara, A.B., Hurlburt, H.E., Rochford, P.A., O'Brien, J.J., 2004. The impact of water turbidity on the interannual sea surface temperature simulations in a layered global ocean model. J. Phys. Oceanogr. 34, 345–359.

Kara, A.B., Wallcraft, A.J., Hurlburt, H.E., 2003. Climatological SST and MLD simulations from NLOM with an embedded mixed layer. J. Atmos. Oceanic Technol. 20, 1616–1632.

Kara, A.B., Rochford, P.A., Hurlburt, H.E., 2002. Air–sea flux estimates and the ENSO event. Bound-Layer Meteor. 103, 439–458.

Large, W.G., McWilliams, J.C., Doney, S., 1994. Oceanic vertical mixing: A review and a model with a nonlocal boundary layer parameterization. Rev. Geophys. 32, 363–403.

Martin, P.J., 2000. Description of the Navy Coastal Ocean Model Version 1.0. NRL Report No. NRL/FR/7322/00/9962, 45 pp. [Available from NRL, Code 7322, Bldg. 1009, Stennis Space Center, MS 39529-5004, USA].

Martin, P., Allard, R.A., 1993. The calculation of solar extinction from satellite color for ocean modeling. NRL Report No. NRL/MR/7322-93-7021, 70 pp. [Available from NRL, Code 7323, Bldg 1009, Stennis Space Center, MS 39529-5004, USA].

Martin, P., 1985. Simulation of the mixed layer at OWS November and Papa with several models. J. Geophys. Res. 90, 903–916.

McCalpin, J.D., 1994. A comparison of second-order and fourth-order pressure gradient algorithms in a sigma-coordinate ocean model. Int. J. Num. Meth. Fluids 18, 361–383.

McPhaden, M.J., Busalacchi, A.J., Cheney, R., Donguy, J.R., Gage, K.S., Halpern, D., Ji, M., Julian, P., Meyers, G., Mitchum, G.T., Niiler, P.P., Picaut, J., Reynolds, R.W., Smith, N., Takeuchi, K., 1998. The Tropical Ocean-Global Atmosphere (TOGA) observing system: A decade of progress. J. Geophys. Res. 103, 14169–14240.

Mellor, G.L., 1991. An equation of state for numerical models of oceans and estuaries. J. Atmos. Oceanic Technol. 8, 609–611.

Mellor, G.L., Blumberg, A.F., 1985. Modeling vertical and horizontal diffusivities with the sigma coordinate system. Mon. Wea. Rev. 113, 1379–1383.

Mellor, G.L., Yamada, T., 1974. A hierarchy of turbulence closure models for planetary boundary layers. J. Atmos. Sci. 31, 1791–1806.

Mellor, G.L., Yamada, T., 1982. Development of a turbulence closure model for geophysical fluid problems. Rev. Geophys. Space Phys. 20, 851–875.

Millero, F.J., Poisson, A., 1981. International one-atmosphere equation of state of seawater. Deep Sea Res. Part I 28, 625–629.

Millero, F.J., Chen, C.-T., Bradshaw, A., Schleicher, K., 1980. A new high pressure equation of state for seawater. Deep Sea Res. Part I 27, 255–264.

Murphy, A.H., 1988. Skill scores based on the mean square error and their relationships to the correlation coefficient. Mon. Wea. Rev. 116, 2417–2424.

Murray, R.J., 1996. Explicit generation of orthogonal grids for ocean models. J. Computat. Phys. 126, 251–273.

Paul, J.F., 1994. Observations related to the use of the sigma coordinate transformation for estuarine and coastal modeling studies. In: Spaulding, M., Bedford, K., Blumberg, A., Cheng, R., Swanson, C. (Eds.), Proceedings, 3rd International Conference on Estuarine and Coastal Modeling III. Amer. Soc. of Civil Eng., New York, p. 682.

Rhodes, R.C., Hurlburt, H.E., Wallcraft, A.J., Barron, C.N., Martin, P.J., Metzger, E.J., Shriver, J.F., Ko, D.S., Smedstad, O.M., Cross, S.L., Kara, A.B., 2002. Navy real-time global modeling systems. Oceanography 15, 29–43.

Rosmond, T.E., Teixeira, J., Peng, M., Hogan, T.F., Pauley, R., 2002. Navy operational global atmospheric prediction system (NOGAPS): Forcing for ocean models. Oceanography 15, 99–108.

Servain, J., Busalacchi, A.J., McPhaden, M.J., Moura, A.D., Reverdin, G., Vianna, M., Zebiak, S.E., 1998. A pilot research moored array in the tropical atlantic (PI-RATA). Bull. Amer. Met. Soc. 79, 2019–2031.

Smagorinsky, J., 1963. General circulation experiments with the primitive equations. I: The basic experiment. Mon. Wea. Rev. 91, 99–164.

Zalesak, S.T., 1979. Fully multidimensional flux-corrected transport algorithms for fluid. J. Comp. Phys. 31, 335–362.